Reduced-order Model for Parameter Tuning of Virtual Synchronous Generator for Desired Frequency Dynamics in Isolated Hybrid Microgrid

Liciane Otremba, Renato M. Monaro, *Member*, *IEEE*, Gilney Damm, *Member*, *IEEE*, and Cristiano M. Verrelli

***Abstract*—The application of a virtual synchronous generator (VSG) to provide virtual inertia in isolated microgrids has emerged as a promising control strategy for converter-interfaced renewable energy sources. However, tuning the VSG parameters requires an accurate characterization of frequency dynamics, which remains a challenge, particularly in hybrid microgrids combining conventional and renewable units. In this context, this paper proposes a reduced-order model to support the parameter tuning of VSGs in an isolated hybrid microgrid composed of an oil and gas facility powered by gas generators connected to an offshore wind turbine. A VSG-based control strategy is applied on the grid-side converter of the wind turbine, allowing it to contribute to frequency regulation and inertia emulation. An analytical formulation is developed to determine the frequency nadir, its time of occurrence, and the rate of change of frequency based on the fixed parameters of the gas generators and the tunable parameters of the VSG. A procedure for parameter tuning to attain the desired frequency dynamics is derived from the analytical formulation. Simulations based on MATLAB/Simulink Simscape Electrical model demonstrate the effectiveness of the proposed procedure by illustrating its consistency in guiding parameter tuning and achieving the desired frequency dynamics.**

***Index Terms*—Microgrid, virtual synchronous generator (VSG), offshore wind turbine, frequency dynamics, parameter tuning, reduced-order model.**

Manuscript received: June 13, 2024; revised: December 25, 2024; accepted: June 17, 2025. Date of CrossCheck: June 17, 2025. Date of online publication: July 24, 2025.

This work was supported in part by Research and Development (R&D) project by Petrobras and the University of São Paulo entitled "Research and Development of Floating Offshore Wind Turbines in Deep Water" (Petrobras Agreement 5900.0112605.19.9), Coordination for the Improvement of Higher Education Personnel - Brasil (CAPES) - Finance Code 001, São Paulo Research Foundation (FAPESP) (#2022/02924-4), and National Council for Scientific and Technological Development (CNPq) (309284/2021-0 and 407723/2021-8). The authors thank Petrobras for funding this project and the National Petroleum Agency (ANP) for providing the regulatory framework under which this funding takes place.

L. Otremba and R. M. Monaro (corresponding author) are with the Laboratory of Advanced Grids (LGrid), Polytechnic School of the University of São Paulo (USP), 05508-010 São Paulo, Brazil (e-mail: liciane.otremba@usp.br; monaro@usp.br).

G. Damm is with the Laboratory Instrumentation, Modélisation, Simulation et Expérimentation (COSYS-IMSE), University Gustave Eiffel, 77420 Marne-la-Vallée, France (e-mail: gilney.damm@univ-eiffel.fr).

C. M. Verrelli is with the Electronic Engineering Department, University of Rome Tor Vergata, 00133 Rome, Italy (e-mail: verrelli@ing.uniroma2.it).

DOI: 10.35833/MPCE.2024.000824

I. Introduction

THE rising trend of replacing fossil fuels with renewable energy sources (RESs) has paved the way for the development of new technologies and different arrangements of grid-connected microgrids and isolated power systems [1]-[3]. However, the variability and uncertainty of RESs in power generation pose some challenges to the system operation. The replacement of conventional generators with converter-interfaced RESs reduces the overall system inertia [4]-[6], as the converter-interfaced RESs lack inherent inertia and primary frequency support [7]. The inertia degradation affects the system dynamic performance and stability owing to a faster rate of change of frequency (ROCOF), creating large frequency deviations [7] and potential failures to respect the limits on grid operation (grid codes) or protection.

As inertial response is an essential element of power generator control [6], different inertia emulation strategies for power converters have been proposed to mimic the inertial response of conventional synchronous generators (SGs) [5], [8]. These power converters can operate in the grid-forming mode and thus participate in the system frequency control [9]. In this scenario, a primary energy source coupled with a short-term energy storage element, a power converter, and control algorithms form a configuration referred to as a virtual inertia system [8]. In this study, the virtual synchronous generator (VSG) topology is based on the synchronverter strategy presented originally in [10].

Unlike conventional SGs, VSGs offer tunable parameters to enhance the system dynamic response. After a large disturbance, the primary frequency support stabilizes the overall frequency, and the prediction of the frequency nadir is essential to ensure sufficient spinning reserve for control action [11]. Hence, predicting the maximum frequency deviation and its time of occurrence is a critical design criterion for operating a microgrid, designing the primary frequency response, and tuning the controller. However, the accurate prediction of the frequency nadir must consider the system-wide frequency response [12]. Various methods have been proposed to describe the frequency dynamics, namely, analytical, simulation, and artificial intelligence methods [11]. The analytical methods, which constitute the scope of this study, directly characterize the frequency dynamics without requir-

ing extensive numerical simulations or complex tools. Details on simulation and artificial intelligence methods can be further found in [13], [14].

The analytical methods commonly simplify the frequency dynamic characteristics to develop a low-order model of the system frequency response. In [15], a low-order model estimates the essential frequency response characteristics, neglecting the generator nonlinearities and focusing on the inertia and time constants of a steam-turbine-based system. In [16], an equivalent dynamic model for average system frequency dynamics is proposed, accounting for the effects of different governor-turbine dynamics for a multimachine system. The frequency nadir prediction method in [11] includes the governor characteristics and considers a parabolic frequency deviation as input, decoupling the governor response calculation and frequency deviation. A two-machine equivalent model in [17] considers a spatiotemporal characteristic to describe the dynamic frequency response and intermachine oscillation. Although different characteristics have been integrated to improve the accuracy of nadir prediction, the existing methods do not focus on tuning system parameters to attain the desired frequency dynamics—a feasible method with VSGs.

Several studies have addressed the emulation of SG dynamics through a control method applied to a power converter with tunable parameters of VSGs. The concept of adaptive virtual inertia in [18], which varies according to the frequency deviation, enhances the frequency regulation in a microgrid. A solution for the improvement of frequency stability is presented in [19], which utilizes an adaptive virtual inertia scheme to promote the stable operation of an AC/DC microgrid with support for ancillary services. An adaptive control strategy with a mutual damping term in a parallel VSG system is proposed in [20], and the effects of the moment of inertia and damping coefficients are also addressed, though without considering the influence of additional machines in the transient response. In [21], an adaptive droop coefficient is proposed for active power and DC voltage in a VSG. Additional parameter adjustments in VSGs include the improvement in dynamic response speed [22], the inclusion of virtual impedance to enhance damping and limit fault current [23], as well as the analytical solution for designing output impedance, inertia constant, and voltage droop [24]. Although a set of guidelines has been established in the literature to design parameters of VSGs, a comprehensive method relating the tunable parameters of VSGs to the frequency nadir in microgrids combining conventional generators and renewable units remains an open topic and represents the main focus of this study.

The hybrid microgrid considered in this study refers to a simplified oil and gas (O&G) facility powered by SGs driven by gas turbines, integrated with an offshore wind turbine, as the RES integration into the O&G exploration sector [1], [25], [26] represents a promising framework for the energy transition. A VSG-based control strategy is applied to the grid-side converter of the wind turbine, allowing it to contribute to frequency regulation and inertia emulation. Considering this scenario, this study develops a systematic procedure for the parameter tuning of the VSG to shape the frequency response into the desired frequency dynamics. Unlike a conventional approach for tuning parameters of VSGs, which relies on detailed electromagnetic transient models and extensive simulations, the proposed analytical formulation aims to reduce the model complexity and computational effort.

The main contributions of this study are highlighted as follows:

1) A reduced-order model for the parameter tuning of the VSG is proposed, and its analytical formulation is developed to determine the frequency nadir, its time of occurrence, and the ROCOF.

2) The analytical formulation allows the parameter tuning of VSGs such as virtual droop and inertia coefficients to shape the frequency response while considering the influence of the governor parameters of a real SG.

3) The proposed procedure for parameter tuning of the VSG is not limited to wind power systems integrated with gas generators. It is also adaptable to alternative energy sources and battery energy storage systems, and may even be broadened to integrate other turbine types, including hydraulic or steam turbines, by modifying the governor model appropriately.

The remainder of this paper is organized as follows. Section II summarizes the main aspects of the isolated hybrid microgrid considered in this study. Section III describes the procedure to define the analytical formulation of the reduced-order model for determining the desired frequency dynamics as a function of the tunable parameters of the VSG. Section IV presents the detailed numerical results. Finally, Section V presents the main conclusions and highlights the specific contributions of this study.

II. Main Aspects of Isolated Hybrid Microgrid Considered in This Study

The configuration of the isolated hybrid microgrid considered in this study is illustrated in Fig. 1, which is based on a realistic scenario provided by industrial partners for validation. It comprises a compact structure of an O&G facility (named floating, production, storage, and offloading (FPSO) system) consisting of an SG driven by the gas turbine and the equivalent model of two induction motors (IMs) and an offshore wind turbine, which are connected by a short submarine cable with impedance Z_{LT} and two transformers (T1 and T2). The following subsections describe the main equipment, control systems, and variables presented in the FPSO system and offshore wind turbine from Fig. 1.

A. FPSO System

The simplified FPSO system is based on the model presented in [27], in which 31.25 MVA, 13.8 kV, 60 Hz gas generators, driven by 25 MW gas turbines, provide electricity to the consuming facilities such as oil extraction, accommodation, processing, exporting, and water and gas re-injections [26]. The load of the FPSO system is mainly represented by the 11 MW, 13.8 kV, and 60 Hz IMs, which operate with a loading of 0.565 p.u.. This study further considers an auxiliary load of 3 MW, 13.8 kV, and 60 Hz for dynamic analysis purposes.

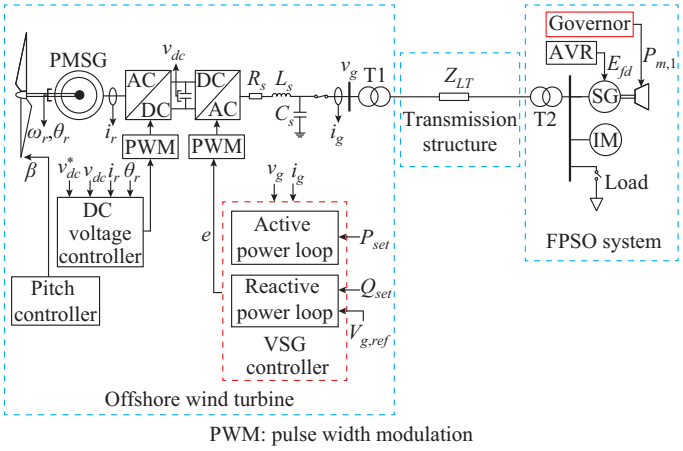

Fig. 1. Configuration of isolated hybrid microgrid considered in this study.

The SG representation comprises the generator model itself and its control systems, including the voltage regulation system—automatic voltage regulator (AVR)—and the speed governor for primary frequency control (PFC). The AVR receives the terminal voltage and field current acting on the generator field winding to adjust the field voltage E_{fd}. The AVR implementation in this study is based on the IEEE Std 421.5-2005 AC8 model [28], associated with an over-excitation limiter.

The speed governor acts over the prime mover to control speed through the fluid intake valve position, adjusting the mechanical power supplied to the SG. Figure 2 illustrates the gas generator governor scheme as a simplification result of the gas generator governor presented in [27]. $K_{1,s}$ and $K_{2,s}$ are the gains corresponding to the tuning parameters to match the governor response; ω_{ref} is the reference value of the gas generator angular speed; ω_1 is the actual angular speed of the gas generator; $P_{ref,1}$ is the power reference; $P_{e,1}$ is the active power; and $P_{m,1}$ is the mechanical power of the gas generator. The frequency error $\omega_1-\omega_{ref}$ is subtracted from the power error signal (between the power reference $P_{ref,1}$ multiplied by the gain K and the input power $P_{e,1}$ multiplied by the governor droop gain $K_{d,1}$). Note that the gain K is set as a unitary value and is only used to match the power signal $P_{ref,1}$ in the sum point. Thus, it is not considered in the formulation development. The resulting signal $\dot{\sigma}_1$ is then used to compute $P_{m,1}$ fed to the SG.

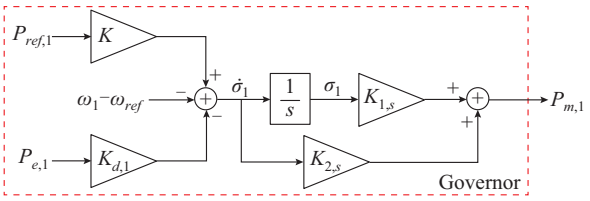

Fig. 2. Gas generator governor scheme.

B. Offshore Wind Turbine

The offshore wind turbine is based on the 15 MW Type IV model specified in the National Renewable Energy Laboratory (NREL) technical report [29]. It is driven by a permanent magnet synchronous generator (PMSG), connected to the grid via a full-scale back-to-back converter, which enables active and reactive power control, smooth grid connection, and generator operation under its full speed range [30]. In addition, variable-speed wind turbines driven by PMSGs correspond to a widely used configuration in offshore applications owing to the absence of the gearbox, which reduces the maintenance costs [31].

From a control perspective, the wind turbine is designed to provide the maximum power available from the wind speed, by utilizing the maximum power point tracking (MPPT) strategy. Conventionally, the grid-side converter controls the DC-link voltage, whereas the rotor-side converter implements the MPPT control [30]. This power electronic interface decouples the generator dynamics from the power system, eliminating the frequency-dependent nature of the PMSG [32]. To enable the participation of the wind turbine in the regulation of the system frequency, a suitable control strategy, emulating an SG, can be applied to the grid-side converter of the wind turbine. In this scenario, the DC-link voltage is controlled by the rotor-side converter, as indicated in Fig. 1, based on the zero-direct current (ZDC) control strategy [30]. The DC voltage controller utilizes the rotor angular position θ_r, obtained from the rotational speed ω_r, generator current i_r, DC-link voltage v_{dc}, and its reference v_{dc}^* as inputs for the control loops.

In this study, the VSG controller for the grid-side converter of the wind turbine is based on the synchronverter arrangement [10], in which the power converter is tied to the grid through an output filter with resistance R_s, inductance L_s, and capacitance C_s, as shown in Fig. 1, and is controlled through active and reactive power loops. The grid voltage v_g and grid current i_g are inputs to the controller, which generates the voltage e applied to the converter. In the active power loop, shown in Fig. 3, the virtual inertia emulation relies on using the swing equation to generate the control signal for the power converter. The parameter M_2 is the virtual inertia coefficient; ω_2 is the VSG angular speed; ω_{grid} is the grid angular speed; θ_2 is the virtual mechanical angle; $P_{m,2}$ is the virtual mechanical power; $P_{e,2}$ is the converter output power; and D_2 is the damping coefficient. In the grid-connected topologies of virtual inertia systems, D_2 is often interpreted as a frequency droop [10], [33], [34], as ω_{grid} is defined as a nonvariable parameter. This assumption is not valid in the application presented herein—where the gas generator and wind turbine form an isolated system—as ω_{grid} varies according to the frequency oscillations.

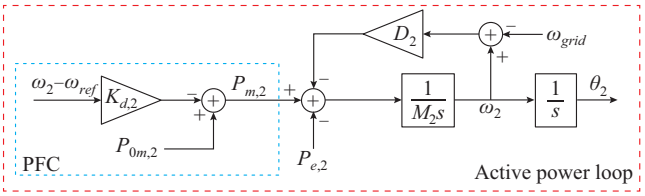

Fig. 3. Simplified scheme modified from [10] of VSG associated with a PFC.

In addition, to enhance frequency regulation, this study im-

plements the PFC as the supplementary loop in Fig. 3 to provide the $P_{m,2}$ signal, which is the mechanical power of the VSG. The parameter $K_{d,2}$ is the virtual droop coefficient, and $P_{0m,2}$ is the mechanical power reference of the VSG (corresponding to P_{set} in Fig. 1). Note that $P_{0m,2}$ is provided by the secondary control action, which is out of the scope of this study. Both inertial and primary frequency responses require that the wind turbine be operated with a power reserve, which can be achieved with a degraded speed (over/under speed) or a pitch deloading action (the relation of VSG parameters and the physical restrictions of the wind turbine shall be the scope of future studies). In this study, the operation of the wind turbine under power reserve is achieved through the overspeed increase in the rotor speed reference in the pitch controller, which, in turn, is based on a simple proportional-integral (PI) control actuating over the pitch angle β (see Fig. 1).

Similar to the AVR operation in a conventional SG, a reactive power loop composes the VSG controller. The implemented reactive power loop is based on the model presented in [10], [33], [34] using the reactive power reference Q_{set} and terminal voltage reference $V_{g,ref}$ as inputs.

III. Analytical Formulation of Reduced-order Model for Determining Desired Frequency Dynamics

A. Swing Equations and Steady-state Frequency Dynamics

A procedure to create an analytical model used to determine the frequency nadir, its time of occurrence, and the ROCOF is proposed based on the two swing equations in (1).

$$\begin{cases} M_1 \dot{\omega}_1 = P_{m,1} - P_{e,1} \\ M_2 \dot{\omega}_2 = P_{m,2} - P_{e,2} \end{cases} \tag{1}$$

where subscript 1 represents the gas generator parameters; subscript 2 represents the VSG parameters; and M_1 is the inertia coefficient from the gas generator.

Three simplifications are made hereafter to obtain a reduced-order model that establishes the influence of tunable parameters on the desired frequency dynamics.

1) Neglect of system losses. The losses in the model depicted in Fig. 1 are disregarded, as a short-line model is utilized to connect the FPSO system to the offshore wind turbine. A small electrical distance (10 km) between the gas generator and the VSG is considered. Nevertheless, these losses may be incorporated into the load variation and have a negligible influence on the model.

2) Assumption of machine coherence. The oscillating power between the gas generator and the VSG is ignored owing to the reduced electrical distance, which allows the assumption that both devices exhibit coherence and oscillate conjointly following a disturbance. This is a conventional procedure even in the analysis of large-scale power systems. These potential oscillations would occur around the overall frequency excursion modeled in this study, and would not significantly alter the overall frequency dynamics.

3) Exclusion of damping coefficients. The damping coefficients for the swing equations of the gas generator and the VSG are omitted (i.e., D_2 is excluded in the formulation), focusing on the dynamic interactions introduced by the control action.

Regarding the equations in (1), which describe the swing dynamics of the gas generator and VSG, the errors $\tilde{\omega}_1$, $\tilde{\omega}_2$, and $e_{p,1}$ are defined to allow a compact notation.

$$\begin{cases} \tilde{\omega}_1 = \omega_1 - \omega_{ref} \\ \tilde{\omega}_2 = \omega_2 - \omega_{ref} \\ e_{p,1} = \dfrac{P_{ref,1}}{K_{d,1}} - P_{e,1} \end{cases} \tag{2}$$

In a strict analogy to the role of $P_{0m,2}$, parameter $P_{0m,1}$ is defined according to (3), and the power error in the gas generator $e_{p,1}$ is redefined in (4).

$$P_{0m,1} = \frac{P_{ref,1}}{K_{d,1}} \tag{3}$$

$$e_{p,1} = P_{0m,1} - P_{e,1} \tag{4}$$

According to (2) - (4), the governor and swing equations for the gas generator and VSG are rewritten as (5).

$$\begin{cases} \dot{\sigma}_1 = K_{d,1}\, e_{p,1} - \tilde{\omega}_1 \\ M_1 \dot{\tilde{\omega}}_1 = K_{1,s}\sigma_1 + \left(K_{2,s}K_{d,1} + 1\right) e_{p,1} - K_{2,s}\tilde{\omega}_1 - P_{0m,1} \\ M_2 \dot{\tilde{\omega}}_2 = P_{0m,2} - K_{d,2}\tilde{\omega}_2 - P_{e,2} \end{cases} \tag{5}$$

As the sum of individual power $P_{e,1}$ and $P_{e,2}$ corresponds to the load demand P_L, as indicated in (6), the power error $e_{p,1}$ in (4) can be rewritten as (7).

$$P_L = P_{e,1} + P_{e,2} \tag{6}$$

$$e_{p1} = P_{0m,1} - P_L + P_{e,2} \tag{7}$$

Assuming, at this stage, that ω_1 and ω_2 swing together (so that $\tilde{\omega}_1 \equiv \tilde{\omega}_2 \equiv \tilde{\omega}$), $P_{e,2}$ is declared as (8).

$$P_{e,2} = P_{0m,2} - K_{d,2}\tilde{\omega} - M_2 \dot{\tilde{\omega}} \tag{8}$$

This assumption, namely, $\tilde{\omega}_1 \equiv \tilde{\omega}_2 \equiv \tilde{\omega}$, relies on a specific physical motivation, neglecting intermachine oscillations owing to the small electrical distance between the generation areas. The approach follows the concept of coherent machines, which considers that SGs swing together after a large power system disturbance [35]. Thereby, the relations in (9) are employed in the following developments.

$$\begin{cases} \omega_1 = \omega_2 \triangleq \omega \\ \tilde{\omega} = \omega - \omega_{ref} \end{cases} \tag{9}$$

The substitution of (8) in (7), and later in the first two equations of (5), leads to a set of relations to characterize $\tilde{\omega}$ as a function of the governor and VSG parameters. Aiming at achieving a more compact notation, new variables such as γ_1 and the modified equivalent inertia coefficient M'_{eq} are defined in (10) and (11), respectively.

$$\gamma_1 = \sigma_1 + K_{d,1} M_2 \tilde{\omega} \tag{10}$$

$$M'_{eq} = M_1 + M_2 + K_{2,s} K_{d,1} M_2 \tag{11}$$

Thus, the overall governor response and the equivalent machine dynamics are expressed by (12).

$$\begin{cases}\dot{\gamma}_1=-\left(K_{d,1}K_{d,2}+1\right)\tilde{\omega}+K_{d,1}\left(P_{0m,1}+P_{0m,2}-P_L\right)\\ M'_{eq}\dot{\tilde{\omega}}=K_{1,s}\gamma_1-\left(\psi+K_{1,s}K_{d,1}M_2\right)\tilde{\omega}+K_{2,s}K_{d,1}P_{0m,1}+\\ \qquad\left(K_{2,s}K_{d,1}+1\right)\left(P_{0m,2}-P_L\right)\end{cases}\tag{12}$$

where $\psi=K_{2,s}+K_{2,s}K_{d,1}K_{d,2}+K_{d,2}$ corresponds to a reparameterization to simplify the notation.

The linear system described in (12) can be synthesized in the standard form:

$$\begin{cases}\dot{\boldsymbol{x}}=\boldsymbol{A}\boldsymbol{x}+\boldsymbol{B}\boldsymbol{u}\\ y=\boldsymbol{C}\boldsymbol{x}\end{cases}\tag{13a}$$

$$\boldsymbol{A}=\begin{bmatrix}0 & -\left(K_{d,1}K_{d,2}+1\right)\\ \dfrac{K_{1,s}}{M'_{eq}} & -\dfrac{\psi+K_{1,s}K_{d,1}M_2}{M'_{eq}}\end{bmatrix}\tag{13b}$$

$$\boldsymbol{B}=\begin{bmatrix}K_{d,1} & K_{d,1} & K_{d,1}\\ \dfrac{K_{2,s}K_{d,1}}{M'_{eq}} & \dfrac{K_{2,s}K_{d,1}+1}{M'_{eq}} & \dfrac{K_{2,s}K_{d,1}+1}{M'_{eq}}\end{bmatrix}\tag{13c}$$

$$\boldsymbol{C}=\begin{bmatrix}0 & 1\end{bmatrix}\tag{13d}$$

$$\boldsymbol{x}=\begin{bmatrix}\gamma_1\\ \tilde{\omega}\end{bmatrix}\tag{13e}$$

$$\boldsymbol{u}=\begin{bmatrix}P_{0m,1}\\ P_{0m,2}\\ -P_L\end{bmatrix}\tag{13f}$$

$$y=\tilde{\omega}\tag{13g}$$

Thus, the steady-state frequency dynamics of the closed-loop system under the predisturbance condition is achieved by regarding $P_{e,1}=P_{0m,1}$ and $P_{e,2}=P_{0m,2}$; thus, $P_L=P_{0m,1}+P_{0m,2}$ for $t\geq t_*$, where t_* is a certain positive real value. Thus, the following equations hold for $t\geq t_*$.

$$P_{0m,1}-P_L+P_{0m,2}=0\tag{14a}$$

$$P_{0m,1}-P_{e,1}+P_{e,1}-P_L+P_{0m,2}=0\tag{14b}$$

$$P_{0m,1}-P_{e,1}+P_{0m,2}-P_{e,2}=0\tag{14c}$$

$$-P_L+P_{0m,2}=-P_{e,1}-P_{e,2}+P_{0m,2}=-P_{e,1}\tag{14d}$$

Now, if the integral error (15) is defined, then (12) becomes (16) for $t\geq t_*$, that is, (17) holds with $\boldsymbol{z}=\left[\tilde{\gamma}_1,\tilde{\omega}\right]^{\mathrm{T}}$.

$$\tilde{\gamma}_1=\gamma_1-\frac{P_{e,1}}{K_{1,s}}\tag{15}$$

$$\begin{cases}\dot{\tilde{\gamma}}_1=-\left(K_{d,1}K_{d,2}+1\right)\tilde{\omega}\\ M'_{eq}\dot{\tilde{\omega}}=-\left(\psi+K_{1,s}K_{d,1}M_2\right)\tilde{\omega}+K_{1,s}\tilde{\gamma}_1\end{cases}\tag{16}$$

$$\dot{\boldsymbol{z}}=\boldsymbol{A}\boldsymbol{z}\tag{17}$$

The time-domain solution given by (18) tends exponentially to zero for any $\boldsymbol{z}(t_*)$, i.e., for any $\tilde{\gamma}_1(t_*)$ and $\tilde{\omega}(t_*)$, and for positive real values $K_{d,2}$ and M_2, as they correspond to the adjustable parameters of the VSG.

$$\boldsymbol{z}(t)=\mathrm{e}^{\boldsymbol{A}(t-t_*)}\boldsymbol{z}(t_*)\tag{18}$$

B. Transient Response Properties

Given the space state in (13), the resulting transfer matrix $\boldsymbol{G}(s)$ is shown in (19).

$$\begin{cases}\boldsymbol{Y}(s)=\boldsymbol{G}(s)\boldsymbol{U}(s)\\ \boldsymbol{G}(s)=\boldsymbol{C}(s\boldsymbol{I}-\boldsymbol{A})^{-1}\boldsymbol{B}\end{cases}\tag{19}$$

where $\boldsymbol{Y}(s)$ is the column vector of the outputs; $\boldsymbol{U}(s)$ is the column vector of the inputs; and $\boldsymbol{I}$ is the identity matrix.

Each element of the transfer matrix $\boldsymbol{G}(s)$ can be described by a second-order transfer function with stable non-coincident poles and a real nonzero zero, whose general form is (20), in which $G_i(s)$ is the element of $\boldsymbol{G}(s)$; λ is the static gain; α_i is a coefficient related to the zero location; ζ is the damping ratio; and ω_n is the undamped natural frequency [36] with a clear physical meaning in the case of complex and conjugate poles. Note that the location of zeros significantly affects the system transient frequency dynamics, for example, increasing the overshoot [36]. Furthermore, the proximity of a zero to a specific pole tends to attenuate the dynamics of that pole [36]. Hence, a suitable fit for the system transient response requires an overall analysis considering both poles and zeros.

$$G_i(s)=\lambda\frac{\dfrac{s}{\alpha_i\zeta\omega_n}+1}{\left(\dfrac{s}{\omega_n}\right)^2+2\zeta\dfrac{s}{\omega_n}+1}\tag{20}$$

Equation (20) is normalized in terms of frequency when $\bar{s}=s/\omega_n$, modifying the time scale in the step response, which leads to the corresponding notation:

$$G_i(\bar{s})=\lambda\frac{\dfrac{\bar{s}}{\alpha_i\zeta}+1}{\bar{s}^2+2\zeta\bar{s}+1}\tag{21}$$

The output profile, once the transient response profiles are exhausted (namely, for the initial time t_0 tending to $-\infty$), can be directly obtained as the inverse Laplace transform of the sum of the products of each transfer function and the corresponding input signal, starting from its Laplace transform.

$$Y(\bar{s})=Y_1(\bar{s})+Y_2(\bar{s})+Y_3(\bar{s})\tag{22}$$

$$\begin{cases}Y_1(\bar{s})=G_1(\bar{s})\mathcal{L}\left[u(1)\right](\bar{s})=\lambda\dfrac{\dfrac{\bar{s}}{\alpha_1\zeta}+1}{\bar{s}^2+2\zeta\bar{s}+1}\mathcal{L}\left[u(1)\right](\bar{s})\\ Y_2(\bar{s})=G_2(\bar{s})\mathcal{L}\left[u(2)\right](\bar{s})=\lambda\dfrac{\dfrac{\bar{s}}{\alpha_2\zeta}+1}{\bar{s}^2+2\zeta\bar{s}+1}\mathcal{L}\left[u(2)\right](\bar{s})\\ Y_3(\bar{s})=G_3(\bar{s})\mathcal{L}\left[u(3)\right](\bar{s})=\lambda\dfrac{\dfrac{\bar{s}}{\alpha_3\zeta}+1}{\bar{s}^2+2\zeta\bar{s}+1}\mathcal{L}\left[u(3)\right](\bar{s})\end{cases}\tag{23}$$

where α_1, α_2, and α_3 are the zero coefficients for the transfer functions $G_1(\bar{s})$, $G_2(\bar{s})$, and $G_3(\bar{s})$, respectively; $u(1)$, $u(2)$, and $u(3)$ are the elements of the input column vector in (13f); and $\mathcal{L}[\cdot]$ is the Laplace operator.

The evaluation under a step response of amplitude ΔP_L is considered, presuming a sudden power variation in the sys-

tem at $t=0$ following the initial time t_0 that, in turn, tends to $-\infty$, whereas the remaining inputs are always maintained constant from t_0. The inputs are then taken as $u(1)=P_{0m,1}$, $u(2)=P_{0m,2}$, and $u(3)=-P_L=-P_{L0}-\Delta P_L 1$, with 1 being the unit step function.

Regarding the constant inputs $P_{0m,1}$, $P_{0m,2}$, $-P_{L0}$ from t_0, the corresponding steady-state responses are simple constants (namely, $\lambda P_{0m,1}$, $\lambda P_{0m,2}$, $-\lambda P_{L0}$, respectively) and can be considered by using the superposition principle. Thus, the corresponding overall contribution to $y=\tilde{\omega}$ before the application of the step disturbance of P_L is zero as $P_{L0}=P_{0m,1}+P_{0m,2}$ in accordance with (14). Nevertheless, the general output expression $y=\tilde{\omega}$ for $t\geq 0$ is the inverse Laplace transform (with normalized time $\bar{t}$) of (24), leading to (recall that the analysis is restricted to the case of noncoincident poles ϕ_1, ϕ_2) (25).

$$-\lambda \frac{\dfrac{\bar{s}}{\alpha_3\zeta}+1}{\bar{s}^2+2\zeta\bar{s}+1}\frac{\Delta P_L}{\bar{s}} \tag{24}$$

$$y(\bar{t})=C_1 e^{\phi_1\bar{t}}+C_2 e^{\phi_2\bar{t}}+C_3 \tag{25}$$

$$C_1=-Z_2 Z_3 \Delta P_L \tag{26a}$$

$$C_2=-Z_2 Z_4 \Delta P_L \tag{26b}$$

$$C_3=Z_1\left(P_{0m,1}+P_{0m,2}-P_{L0}-\Delta P_L\right)=-Z_1\Delta P_L \tag{26c}$$

$$Z_1=\lambda \tag{27a}$$

$$Z_2=-\frac{\lambda}{2\alpha_3\zeta\sqrt{\zeta^2-1}} \tag{27b}$$

$$Z_3=1-\alpha_3\zeta^2+\alpha_3\zeta\sqrt{\zeta^2-1} \tag{27c}$$

$$Z_4=-1+\alpha_3\zeta^2+\alpha_3\zeta\sqrt{\zeta^2-1} \tag{27d}$$

$$\phi_1=-\zeta-\sqrt{\zeta^2-1} \tag{27e}$$

$$\phi_2=-\zeta+\sqrt{\zeta^2-1} \tag{27f}$$

Thus, $y(0)=C_1+C_2+C_3=0$ in accordance with the previous computations and reasoning.

An analysis of (25) yields the characterization of two significant parameters, namely, the maximum frequency deviation and its time of occurrence. The time-domain solution for the normalized peak time $\bar{t}_p$, which represents the required time for the response to achieve the first peak value, is given by (28), which leads to (29).

$$\left.\frac{dy}{d\bar{t}}\right|_{\bar{t}=\bar{t}_p}=0 \tag{28}$$

$$\bar{t}_p=\frac{\ln\left(-\dfrac{C_1\phi_1}{C_2\phi_2}\right)}{\phi_2-\phi_1} \tag{29}$$

The load-variation-dependent characteristic is eliminated when the equations in (26) and (27) are substituted in (28), which indicates that the time of maximum frequency deviation does not depend on the power imbalance.

The maximum overshoot M_p, i.e., the maximum peak value of the response curve measured from the desired response of the system [37], is obtained by substituting (29) into (25), resulting in (30).

$$M_p=C_1\left(-\frac{C_1\phi_1}{C_2\phi_2}\right)^{-\frac{\phi_1}{\phi_1-\phi_2}}+C_2\left(-\frac{C_1\phi_1}{C_2\phi_2}\right)^{-\frac{\phi_2}{\phi_1-\phi_2}}+C_3 \tag{30}$$

Note that the frequency nadir prediction is directly related to the parameters of transient response λ, ζ, and α_3, indicated in (27). However, a relationship must be established between the general transient response parameters and the control ones that characterize the system frequency dynamics regarding the studied case. Thus, the application of (19) from the state-space defined in (13) results in the following form:

$$\mathcal{L}[\tilde{\omega}](s)=\left[G_1(s),G_2(s),-G_3(s)\right]\begin{bmatrix}P_{0m,1}\\P_{0m,2}\\P_{L0}+\Delta P_L\end{bmatrix} \tag{31}$$

$$G_1(s)=\frac{K_{d,1}K_{2,s}s+K_{d,1}K_{1,s}}{m(s)} \tag{32}$$

$$G_2(s)=G_3(s)=\frac{\left(1+K_{2,s}K_{d,1}\right)s+K_{1,s}K_{d,1}}{m(s)} \tag{33}$$

$$m(s)=M'_{eq}s^2+\left(\psi+K_{1,s}K_{d,1}M_2\right)s+K_{1,s}\left(K_{d,1}K_{d,2}+1\right) \tag{34}$$

The correspondence between the parameters of transient response, i.e., α_i, λ, ζ, and ω_n, and the parameters that define the system frequency dynamics, i.e., $K_{d,1}$, $K_{d,2}$, $K_{1,s}$, $K_{2,s}$, M_1, and M_2, is achieved by comparing (22) and (33) with the general transfer function form presented in (20), which leads to:

$$\lambda=\frac{K_{d,1}}{1+K_{d,1}K_{d,2}} \tag{35}$$

$$\alpha_1=\frac{2K_{1,s}M'_{eq}}{K_{2,s}\left(\psi+K_{1,s}K_{d,1}M_2\right)} \tag{36}$$

$$\alpha_2=\alpha_3=\frac{2K_{1,s}K_{d,1}M'_{eq}}{\left(1+K_{2,s}K_{d,1}\right)\left(\psi+K_{1,s}K_{d,1}M_2\right)} \tag{37}$$

$$\zeta=\frac{\psi+K_{1,s}K_{d,1}M_2}{2\sqrt{M'_{eq}K_{1,s}\left(1+K_{d,1}K_{d,2}\right)}} \tag{38}$$

$$\omega_n=\sqrt{\frac{K_{1,s}\left(1+K_{d,1}K_{d,2}\right)}{M'_{eq}}} \tag{39}$$

Additionally, from (25), the derivative of the frequency response can be computed. A time correction is first applied to (25), resulting in (40), for which the ROCOF is computed as the derivative of the frequency at $t=0$, as indicated in (41), which, in the case of the maximum contingency ($\Delta P_L=P_{\max}$), denotes $ROCOF_{\max}$.

$$y(t)=C_1 e^{\phi_1 t\omega_n}+C_2 e^{\phi_2 t\omega_n}+C_3 \tag{40}$$

$$\left.\frac{dy}{dt}\right|_{t=0}=C_1\phi_1\omega_n+C_2\phi_2\omega_n \tag{41}$$

Finally, the frequency indicators are presented in (42) - (44). The time of minimum frequency occurrence in (42) is

obtained from (29), after correcting the time-scale effect owing to the frequency normalization in (21), and considering a generic disturbance initial time t_d. The frequency nadir (43) (minimum frequency point) is obtained from the expression in (30) and considering the frequency reference value ω_{ref}. The ROCOF (44) is a direct result of applying the transient parameters in (41).

$$t_p = \frac{\bar{t}_p}{\omega_n} + t_d \tag{42}$$

$$N_d = M_p + \omega_{ref} \tag{43}$$

$$ROCOF = -\frac{\lambda}{\alpha_3 \zeta}\omega_n \Delta P_L \tag{44}$$

C. Role and Tuning of Control Parameters

The relations in (35)-(39) comprise a valuable tool to determine the effect of control parameters on the transient response. As the gas generator parameters are fixed and specified by the manufacturer, the parameters of the VSG can be adjusted to shape the dynamic behavior. In this study, the virtual droop coefficient $K_{d,2}$ and virtual inertia coefficient M_2 are tunable parameters whose adjustment affects the frequency nadir and its time of occurrence. Remarkably, the coefficient λ only depends on the droop characteristics regarding its influence on the steady-state error. The coefficient α_i and damping factor ζ are critical in the system overshoot characterization, with $K_{d,2}$ significantly influencing the magnitude of α_i. The damping factor ζ is affected by both parameters $K_{d,2}$ and M_2. However, the underdamped characteristic of the transient response is more affected as $K_{d,2}$ becomes smaller. Moreover, the virtual droop and inertia coefficients influence the natural frequency ω_n.

Although determining the adjustment for $K_{d,2}$ and M_2 for a particular frequency nadir is possible by the numerical solution of (30), this study considers Procedure 1 below, based on the steady-state error to determine $K_{d,2}$ and setting a range of M_2, for which M_p and t_p are obtained, given the system power imbalance ΔP_L.

Procedure 1

Step 1: define the maximum steady-state error λ for a given ΔP_L.

Step 2: find minimum $K_{d,2}$ from (35).

Step 3: set a range of n values for M_2.

Step 4: for each M_2 value from *Step 3*, calculate the transient response parameters from (25a)-(25c), (26a)-(26f), and (35)-(39).

Step 5: obtain the frequency indicators, i.e., time of minimum frequency occurrence (42), minimum frequency (43), and ROCOF (44).

IV. Numerical Results

This section illustrates the frequency dynamics obtained using the proposed procedure. A test case of load connection in the system shown in Fig. 1 is performed to analyze the frequency dynamics and interaction between the gas generator and the VSG. According to Fig. 4, a minor oscillation appears in the gas generator frequency ω_1 and VSG frequency ω_2. However, a common frequency can be derived from the center of inertia (COI) concept according to (45), where p is the number of synchronous generating units (both real and virtual machines); M_i is the individual inertia coefficient; M_T is the total inertia; ω_i is the individual frequency; and ω_{COI} is the COI frequency. Figure 4 indicates that ω_{COI} is consistent with the overall frequency dynamics. Thus, the following analyses consider the COI frequency.

$$\begin{cases} \omega_{COI} = \dfrac{1}{M_T}\displaystyle\sum_{i=1}^{p} M_i \omega_i \\ M_T = \displaystyle\sum_{i=1}^{p} M_i \end{cases} \tag{45}$$

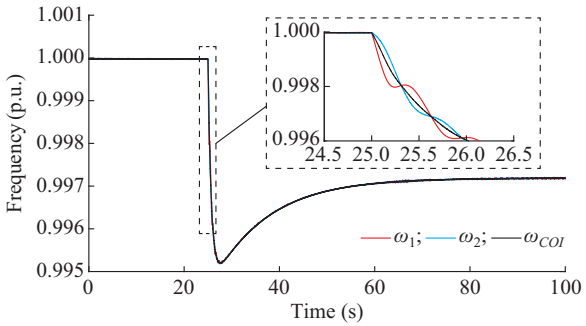

Fig. 4. Frequency dynamics of generation units and system COI.

A brief discussion regarding the cable length variation over the frequency dynamics is presented in Supplementary Material A.

Proceeding to a system dynamic analysis, the system data are converted to the power base of the gas generator (31.25 MVA), and an initial power demand of 0.4839 p.u. (two 11 MW IMs at 0.565 p.u. mechanical power plus the system power losses) is considered. It is further assumed that the wind turbine operates in the overspeed mode for a wind speed of 9 m/s (deloaded operation) and provides 7 MW power to the system. The gas generator supplies the remaining power. The implemented scenarios consider an increase of 3 MW in the power demand applied as a load step. The gas generator governor parameters $K_{1,s}$, $K_{2,s}$, $K_{d,1}$, and M_1 are assumed as constants, and their values are presented in Appendix A, in addition to the cables, power transformers, and VSG output filter parameters. As a project criterion, the parameters of the VSG $K_{d,2}$ and M_2 can be adjusted to achieve a specific performance.

A. Effect of Parameter Variation

Initially, the effect of variation of $K_{d,2}$ and M_2 on the maximum overshoot M_p and peak time $\bar{t}_p$ related to $\tilde{\omega}$ is evaluated assuming only the load effect in the transient response. The range of $K_{d,2}$ is set for three different inertia coefficients regarding the VSG. The resulting parameters λ, α_i, ζ, and ω_n are substituted in (29) and (30), and the effects on $\bar{t}_p$ and M_p are shown in Figs. 5 and 6, respectively. The results indicate a significant effect of both parameters, $K_{d,2}$ and M_2, on the peak time, according to the curves in Fig. 5. The increase in the inertia coefficient leads to a delay in reaching the maximum overshoot owing to the ROCOF variation, consequently raising the peak time. However, the increase in $K_{d,2}$ tends to minimize the inertia effect on $\bar{t}_p$. This droop superimpos-

ing effect on the inertia is even more relevant for the amplitude of maximum frequency deviation, as presented in Fig. 6.

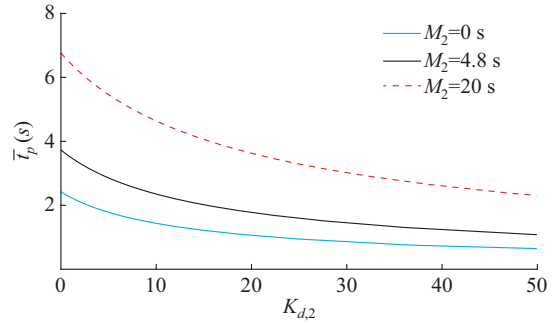

Fig. 5. Effects of $K_{d,2}$ and M_2 on $\bar{t}_p$.

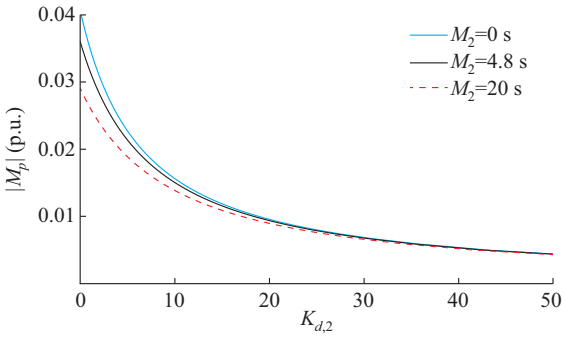

Fig. 6. Effects of $K_{d,2}$ and M_2 on M_p.

Aiming to validate the analytical formulation for the peak time and amplitude of the frequency nadir, a range of simulations is proposed based on the MATLAB/Simulink Simscape Electrical model of the isolated hybrid microgrid presented in Fig. 1. The modeling of the wind turbine comprises the drivetrain (modeled according to [38] based on the two-mass model), PMSG, pitch control system (according to [39]), and back-to-back voltage source converter. The gas generator includes the SG and its control systems regulating the frequency and voltage of the FPSO system. The load representation in the FPSO system includes the IM engines, characterized as an equivalent double squirrel-cage rotor model, and the spot load represented as a constant impedance model. The simulation scenarios consider a load-step of 0.096 p.u. at t_d= 25 s, in which the dynamic response of the frequency is evaluated under different values of $K_{d,2}$ and M_2.

The variation in the virtual inertia coefficient M_2 considering a nonzero $K_{d,2}$ is set, and the frequency dynamics regarding different M_2 and $K_{d,2}=20$ are presented in Fig. 7.

In this case, both generation units, gas turbine and wind turbine, participate in frequency regulation through the PFC action. Considering the virtual droop coefficient as 5%, corresponding to $K_{d,2}=20$, the change in M_2 indicates a minor effect on the frequency nadir. Although the effect of increasing the inertia coefficient on the ROCOF can be observed, as presented in detail in Fig. 7, the droop effect regarding the VSG minimizes the inertia effect on the frequency nadir. The same system conditions are specified as input to (42) and (43), aiming to validate the formulations. The comparison of simulated results obtained by the MATLAB/Simulink Simscape Electrical model and analytical results obtained by the proposed analytical formulation for N_d and t_p regarding different M_2 and $K_{d,2}=20$ is presented in Fig. 8, in which the maximum Euclidean distance corresponds to 0.0344. The comparison of simulated and analytical results for ROCOF regarding different M_2 and $K_{d,2}=20$ is presented in Table I and indicates a maximum relative error of 7.97%.

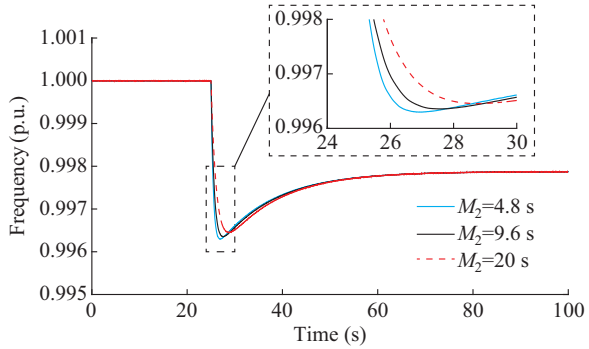

Fig. 7. Frequency dynamics regarding different M_2 and $K_{d,2}=20$.

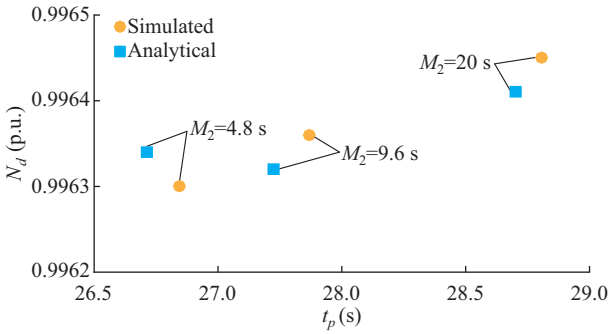

Fig. 8. Comparison of simulated and analytical results for N_d and t_p regarding different M_2 and $K_{d,2}=20$.

TABLE I
COMPARISON OF SIMULATED AND ANALYTICAL RESULTS FOR ROCOF REGARDING DIFFERENT M_2 AND $K_{d,2}=20$

M_2 (s)	ROCOF (p.u./s)		Relative error (%)
	Simulated	Analytical	
4.8	–0.00915	–0.00936	2.30
9.6	–0.00660	–0.00647	1.97
20.0	–0.00414	–0.00381	7.97

Figure 9, obtained from the MATLAB/Simulink Simscape Electrical model, illustrates a comparison with the absence of PFC ($K_{d,2}=0$) for the same inertia coefficients.

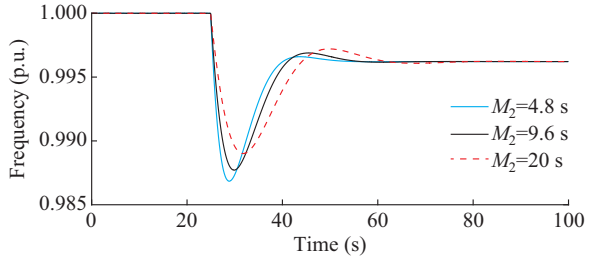

Fig. 9. Frequency dynamics regarding different M_2 and $K_{d,2}=0$.

In this case, the variation in the inertia coefficient significantly affects the frequency nadir and its time of occurrence. The inertia increase indicates a reduction in the ROCOF, as expected, and the frequency nadir is reduced as the system equivalent inertia tends to rise, whereas the peak time increases. The effects of inertia on the frequency performance constitute a relevant strategy to restrict the frequency variation in power systems and further contribute to the system stability. The comparison of simulated and analytical results for N_d and t_p regarding different M_2 and $K_{d,2}=0$ is illustrated in Fig. 10, in which the maximum Euclidean distance corresponds to 0.0311. Further, the comparison of simulated and analytical results for ROCOF regarding different M_2 and $K_{d,2}=0$ in Table II indicates a maximum relative error of 12.85%.

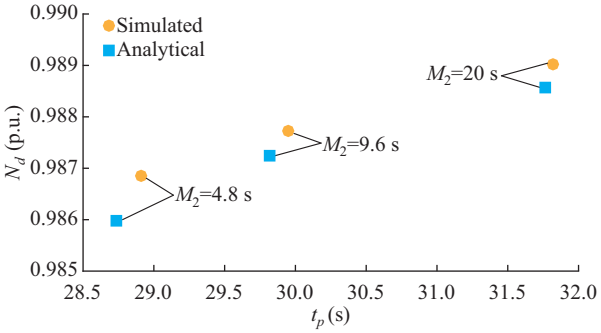

Fig. 10. Comparison of simulated and analytical results for N_d and t_p regarding different M_2 and $K_{d,2}=0$.

TABLE II
COMPARISON OF SIMULATED AND ANALYTICAL RESULTS FOR ROCOF REGARDING DIFFERENT M_2 AND $K_{d,2}=0$

M_2 (s)	ROCOF (p.u./s)		Relative error (%)
	Simulated	Analytical	
4.8	–0.00957	–0.00931	2.72
9.6	–0.00716	–0.00624	12.85
20.0	–0.00424	–0.00375	11.56

Additional analyses are demonstrated for the simulations in MATLAB/Simulink software regarding $K_{d,2}=20$ and $K_{d,2}=0$ cases for $M_2=4.8$ s. As indicated in Fig. 11, the effect of the variation in $K_{d,2}$ significantly influences the frequency nadir for the same inertia coefficient.

The control droop from the VSG side limits the frequency deviation and curbs the frequency nadir. The frequency dynamics depend on how the power is managed from both generation units. In the $K_{d,2}=0$ case, an increase in the generated power from the gas generator $P_{m,1}$ (see Fig. 12(a)) satisfies the load step P_L (see Fig. 12(b)), as the mechanical power from the wind unit $P_{m,2}$ is maintained constant in Fig. 12(c). In the $K_{d,2}=20$ case, additional power supply is required from the wind turbine, which is achieved by reducing its overspeed margin. Further results illustrating the dynamics of the gas generator terminal voltage, wind turbine rotational speed, and DC-link voltage are presented in Supplementary Material B.

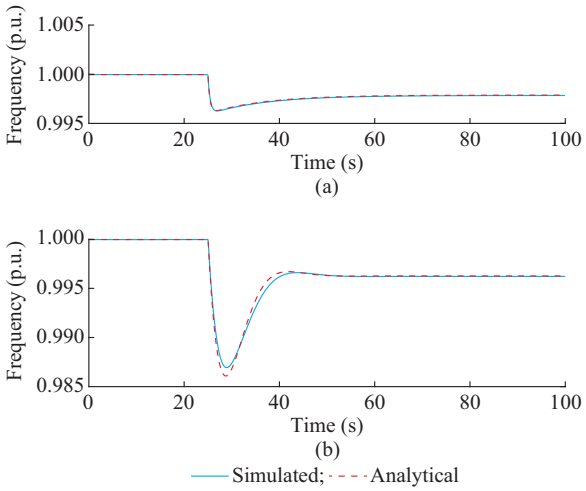

Fig. 11. Comparison of simulated and analytical results for frequency dynamics regarding $M_2=4.8$ s and different $K_{d,2}$. (a) $K_{d,2}=20$. (b) $K_{d,2}=0$.

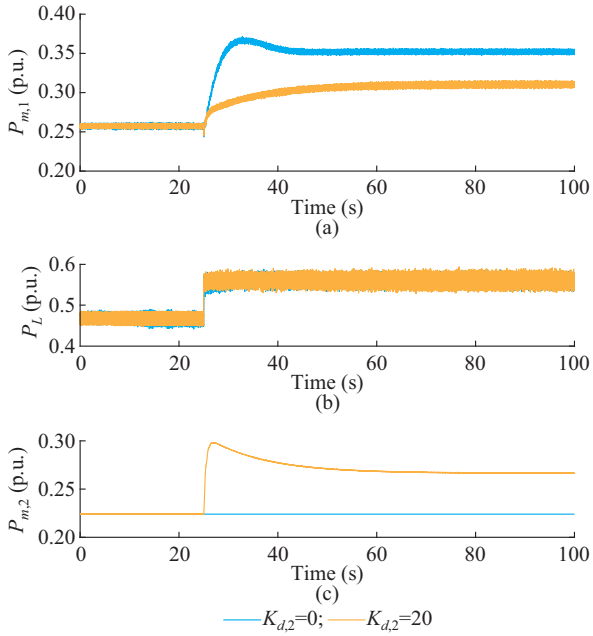

Fig. 12. Performance of system variables regarding mechanical power of gas generator, load demand at FPSO system, and mechanical power of VSG. (a) Mechanical power of gas generator. (b) Load demand at FPSO system. (c) Mechanical power of VSG.

B. Project Design

Based on the previous analysis and the definition of transient response parameters, this subsection presents a sequence of steps, based on Procedure 1, to determine $K_{d,2}$ and M_2 according to the desired frequency dynamics.

1) Defining the maximum steady-state error. A desired steady-state error is a project criterion for the maximum power imbalance. Initially, a load variation of 0.1259 p.u. is established, and a steady-state error of 0.003 p.u. is defined. The frequency deviation response in the steady-state, according to (25), results in (46).

$$y(t)=C_3=-Z_1\Delta P_L=-\lambda\Delta P_L \tag{46}$$

2) Determining the minimum value of $K_{d,2}$. The steady-

state criterion in the previous step leads to a minimum value of $K_{d,2}$. As the parameter λ directly relates to the steady-state frequency deviation, the specified $K_{d,2}$ leads to an adequate primary frequency response. From (46), λ is obtained, and, with the expression in (35), $K_{d,2}$ is achieved. In this example, $\lambda = 0.0238$ and $K_{d,2} = 16.9667$.

3) Obtaining M_2. The value of M_2 for a particular M_p can be obtained from a numerical solution of (30) or from a graphical approach for a range of inertia coefficients, which are evaluated to assure the maximum frequency deviation M_p, according to (30). Hereafter, the graphical approach is chosen to demonstrate the correlation between M_2 and M_p. Equation (30), which relates the adjustable parameters of the VSG to the maximum frequency deviation, is solved from $K_{d,2}$ obtained previously and for a range of n values for M_2. A variation in the virtual inertia coefficient from 0 to 20 s is considered to obtain the analytical results of M_p, as presented in Fig. 13.

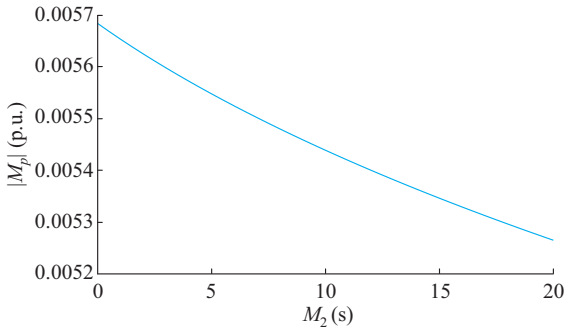

Fig. 13. Analytical results of M_p.

4) Adopting a specific M_2. A specific case of $M_2 = 10$ s is chosen and the simulated result using the MATLAB/Simulink Simscape Electrical model for frequency dynamics is presented in Fig. 14. The simulated results correspond to $t_p = 27.75685$ s and $N_d = 0.99464$ p.u., whereas the analytical results correspond to $t_p = 27.6332$ s and $N_d = 0.9946$ p.u.. This indicates that the desired frequency dynamics are fully obtained by following the proposed procedure for setting the parameter values.

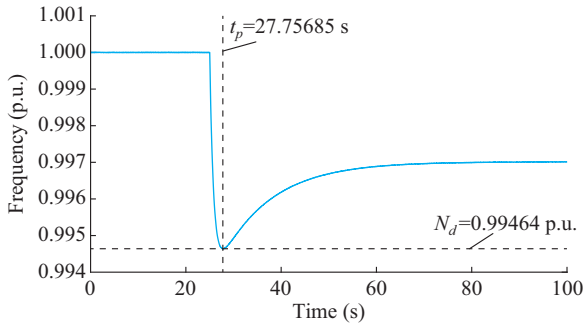

Fig. 14. Frequency dynamics for $M_2 = 10$ s.

As indicated in Fig. 13, there is a slight variation in the possible maximum frequency deviations for the proposed range of inertia coefficients. The frequency dynamics indicate that the droop effect strongly influences the transient response and suppresses the inertia variation effect regarding the VSG. However, note that distinct combinations of $K_{d,2}$ and M_2 can satisfy a specific transient response criterion, which requires a multi-objective approach to parameter tuning.

V. Conclusion and Future Scope

This study considers an isolated system driven by conventional synchronous (gas) generators and an offshore wind turbine. A virtual inertia control based on the synchronverter strategy is implemented on the converter connecting the wind turbine to the isolated hybrid microgrid, which allows for frequency and inertial support from the RES operating in the grid-forming mode. This study considers proposing parameter tuning guidelines for the VSG to attain the desired frequency dynamics. Therefore, an analytical formulation is developed to determine the frequency nadir, its time of occurrence, and the ROCOF as a function of the tunable parameters for the VSG.

The developed formulation shows a direct relationship between the control parameters (e. g., inertia coefficients and droop parameters) and the gas generator governor described by a second-order dynamic equation. A reduced-order model for the entire system is then developed, which is well suited for control design and mathematical analysis. This model highlights and isolates the effects of control parameters of the overall frequency dynamics, which, in turn, allows identifying the specific contribution of such control parameters and the system output. Thus, it is possible to identify the suitable parameter tuning for the desired frequency dynamics. Although a direct implication of grid codes is not addressed in this study, note that the proposed analytical formulation for the tunable parameters $K_{d,2}$ and M_2 can support compliance with the frequency criteria.

The simulation results comparing the proposed model and the MATLAB/Simulink Simscape Electrical model show that the proposed analytical formulation is accurate. Furthermore, this reduced-order model can be adapted to different system configurations and governor topologies. The scenarios simulated consider a variation of virtual droop and virtual inertia coefficients, indicating that the virtual droop coefficient strongly influences the frequency deviation and suppresses the inertia variation effect.

Finally, the proposed procedure is verified using an example in which a desired maximum frequency deviation is set for a given contingency on the grid. The control parameters are tuned following the proposed procedure, and the simulation results show good precision. These results also validate the possibility of using wind power generation for frequency and inertia support for an offshore platform. Therefore, the utility of the proposed procedure relies on its ability to establish a set of parameters to attain the desired frequency dynamics.

In future studies, the physical restrictions of the wind turbine shall be associated with the parameters of the VSG, aiming to establish a limited variation range for droop and inertia coefficients. Moreover, the mathematical development could consider simplifications regarding electrical losses,

damping effects, and machine coherence. Expanding the analysis to include the aforementioned effects can be considered to evaluate the model adequacy for a wide range of grid topologies.

APPENDIX A

1) Parameters of transformers

The rated power, rated voltage, resistance, and leakage reactance of the transformer T1 are 17.5 MVA, 13.8/66 kV, $R=0.3\%$, and $X=10\%$, respectively. The rated power, rated voltage, resistance, and leakage reactance of the transformer T2 are 17.5 MVA, 66 kV/8.26 kV, $R=0.3\%$, and $X=10\%$, respectively.

2) Parameters of cables

The resistance, reactance, and length of the cable are $R_{LT}=0.058$ Ω/km, $X_{LT}=0.1395$ Ω/km, and $l=10$ km, respectively.

3) Parameters of gas generator

$M_1=6.4$ s, $K_{d,1}=0.04$, $K_{1,s}=1.4$, and $K_{2,s}=5.6$.

4) Parameters of VSG output filter

$R_s=0.1423$ Ω, $L_s=60.363$ μH, and $C_s=139.88$ μF.

REFERENCES

[1] S. Sanchez, E. Tedeschi, J. Silva *et al*., "Smart load management of water injection systems in offshore oil and gas platforms integrating wind power," *IET Renewable Power Generation*, vol. 11, no. 9, pp. 1153-1162, Jul. 2017.

[2] C. Wang, J. Li, and Y. Hu, "Frequency control of isolated wind-diesel microgrid power system by double equivalent-input-disturbance controllers," *IEEE Access*, vol. 7, pp. 105617-105626, Aug. 2019

[3] J. M. Rey, G. A. Vera, P. Acevedo-Rueda *et al*., "A review of microgrids in Latin America: laboratories and test systems," *IEEE Latin America Transactions*, vol. 20, pp. 1000-1011, Jun. 2022.

[4] J. Matevosyan, S. Sharma, S. H. Huang *et al*., "Proposed future ancillary services in electric reliability council of Texas," in *Proceedings of 2015 IEEE Eindhoven PowerTech*, Eindhoven, Netherlands, Jun.-Jul. 2015, pp. 1-6.

[5] U. Tamrakar, D. Shrestha, M. Maharjan *et al*., "Virtual inertia: current trends and future directions," *Applied Sciences*, vol. 7, no. 7, p. 654, Jul. 2017.

[6] P. Denholm, T. Mai, R. W. Kenyon *et al*., "Inertia and the power grid: a guide without the spin," NREL, Golden, Tech. Rep., May 2020.

[7] A. Fernández-Guillamón, E. Gómez-Lázaro, E. Muljadi *et al*., "Power systems with high renewable energy sources: a review of inertia and frequency control strategies over time," *Renewable and Sustainable Energy Reviews*, vol. 115, p. 109369, Nov. 2019.

[8] K. S. Ratnam, K. Palanisamy, and G. Yang, "Future low-inertia power systems: requirements, issues, and solutions – a review," *Renewable and Sustainable Energy Reviews*, vol. 124, p. 109773, May 2020.

[9] M. M. Islam, K. M. Muttaqi, D. Sutanto *et al*., "Design of a controller for grid forming inverter-based power generation systems," *IEEE Access*, vol. 11, pp. 55755-55770, May 2023.

[10] Q.-C. Zhong and T. Hornik, *Synchronverters: Grid-friendly Inverters that Mimic Synchronous Generators*. Hoboken: John Wiley & Sons, 2012, pp. 277-296.

[11] L. Liu, W. Li, Y. Ba *et al*., "An analytical model for frequency nadir prediction following a major disturbance," *IEEE Transactions on Power Systems*, vol. 35, no. 4, pp. 2527-2536, Jul. 2020.

[12] S. Yang, Q. Meng, Y. Zhang *et al*., "Simplified prediction model of frequency nadir for power systems penetrated with renewable energy," in *Proceedings of 2022 IEEE PES General Meeting*, Denver, USA, Jul. 2022, pp. 1-5.

[13] G. Kou, P. Markham, S. Hadley *et al*., "Impact of governor deadband on frequency response of the U. S. eastern interconnection," *IEEE Transactions on Smart Grid*, vol. 7, no. 3, pp. 1368-1377, May 2016.

[14] R. F. Chang, C. N. Lu, and T. Y. Hsiao, "Prediction of frequency response after generator outage using regression tree," *IEEE Transactions on Power Systems*, vol. 20, no. 4, pp. 2146-2147, Nov. 2005.

[15] P. M. Anderson and M. Mirheydar, "A low-order system frequency response model," *IEEE Transactions on Power Systems*, vol. 5, no. 3, pp. 720-729, Aug. 1990.

[16] M. Chan, R. Dunlop, and F. Schweppe, "Dynamic equivalents for average system frequency behavior following major distribances," *IEEE Transactions on Power Apparatus and Systems*, vol. PAS-91, no. 4, pp. 1637-1642, Jul. 1972.

[17] J. Shen, W. Li, L. Liu *et al*., "Frequency response model and its closed-form solution of two-machine equivalent power system," *IEEE Transactions on Power Systems*, vol. 36, no. 3, pp. 2162-2173, May 2021.

[18] X. Hou, Y. Sun, X. Zhang *et al*., "Improvement of frequency regulation in VSG-based AC microgrid via adaptive virtual inertia," *IEEE Transactions on Power Electronics*, vol. 35, pp. 1589-1602, Feb. 2020.

[19] F. Perez, G. Damm, C. M. Verrelli *et al*., "Adaptive virtual inertia control for stable microgrid operation including ancillary services support," *IEEE Transactions on Control Systems Technology*, vol. 31, no. 4, pp. 1552-1564, Jul. 2023.

[20] X. Gao, D. Zhou, A. Anvari-Moghaddam *et al*., "An adaptive control strategy with a mutual damping term for paralleled virtual synchronous generators system," *Sustainable Energy, Grids and Networks*, vol. 38, p. 101308, Jun. 2024.

[21] T. University, R. Wang, L. Chen *et al*., "VSG-based adaptive droop control for frequency and active power regulation in the MTDC system," *CSEE Journal of Power and Energy Systems*, vol. 3, no. 3, pp. 260-268, Oct. 2017.

[22] S. Dong and Y. Chen, "Adjusting synchronverter dynamic response speed via damping correction loop," *IEEE Transactions on Energy Conversion*, vol. 32, no. 2, pp. 608-619, Jun. 2017.

[23] B. Rathore, S. Chakrabarti, and L. Srivastava, "A self-regulated virtual impedance control of VSG in a microgrid," *Electric Power Systems Research*, vol. 197, p. 107289, Aug. 2021.

[24] A. Gonzalez-Cajigas, J. Roldan-Perez, and E. J. Bueno, "Design and analysis of parallel-connected grid-forming virtual synchronous machines for island and grid-connected applications," *IEEE Transactions on Power Electronics*, vol. 37, no. 5, pp. 5107-5121, May 2022.

[25] J. Z. Tee, K. H. Tan, I. L. H. Lim *et al*., "Integration of offshore wind with O&G platforms with an energy storage system," in *Proceedings of 2019 IEEE PES Innovative Smart Grid Technologies Europe (ISGT-Europe)*, Bucharest, Romania, Oct. 2019, pp. 1-5.

[26] G. Shi, S. Peng, X. Cai *et al*., "Grid integration of offshore wind farms and offshore oil/gas platforms," in *Proceedings of the 7th International Power Electronics and Motion Control Conference*, Harbin, China, Jun. 2012, pp. 1301-1305.

[27] J. A. Calderon, J. J. Orozco, C. A. V. Guerrero *et al*., "Dynamic control validation of the power generation system of an offshore platform through real-time digital simulation," in *Proceedings of 2021 14th IEEE International Conference on Industry Applications*, São Paulo, Brazil, Aug. 2021, pp. 932-939.

[28] *IEEE Recommended Practice for Excitation System Models for Power System Stability Studies*, IEEE Std 421.5-2005 (Revision of IEEE Std 421.5-1992), 2006.

[29] E. Gaertner, J. Rinker, L. Sethuraman *et al*., "Definition of the IEA 15-megawatt offshore reference wind," NREL, Golden, Tech. Rep., Mar. 2020.

[30] B. Wu, Y. Lang, N. Zargari *et al*., *Power Conversion and Control of Wind Energy Systems*. Hoboken: John Wiley & Sons, 2011.

[31] O. Anaya-Lara, J. O. Tande, K. Uhlen *et al*., *Offshore Wind Energy Technology*. Hoboken: John Wiley & Sons Ltd., 2018.

[32] K. R. Vasudevan, V. K. Ramachandaramurthy, T. S. Babu *et al*., "Synchronverter: a comprehensive review of modifications, stability assessment, applications and future perspectives," *IEEE Access*, vol. 8, pp. 131565-131589, Jul. 2020

[33] Q. Zhong, Z. Ma, W. Ming *et al*., "Grid-friendly wind power systems based on the synchronverter technology," *Energy Conversion and Management*, vol. 89, pp. 719-726, Jan. 2015.

[34] Q. Zhong, "Virtual synchronous machines: a unified interface for grid integration," *IEEE Power Electronics Magazine*, vol. 3, no. 4, pp. 18-27, Dec. 2016.

[35] J. J. Grainger and W. D. J. Stevenson, *Power System Analysis*. Singapore: McGraw-Hill, Inc., 1994, pp. 702-707.

[36] G. F. Franklin, J. D. Powell, and A. Emami-Naeini, *Feedback Control of Dynamic Systems*. London: Pearson, 2014, pp. 137-146.

[37] K. Ogata, *Modern Control Engineering*. London: Pearson, 2009, pp. 164-179.

[38] J. Guo and X. Wang, "The speed control of a direct-drive PMSG-based wind energy conversion system," in *Proceedings of the 27th Chinese Control and Decision Conference*, Qingdao, China, May 2015, pp. 1921-1925.

[39] N. J. Abbas, D. S. Zalkind, L. Pao *et al*., "A reference open-source controller for fixed and floating offshore wind turbines," *Wind Energy Science*, vol. 7, no. 1, pp. 53-73, Jan. 2022.

Liciane Otremba received the B.Sc. and M.Sc. degrees in electrical engineering from the State University of Western Paraná, Foz do Iguaçu, Brazil, in 2017 and 2020, respectively, and the Ph.D. degree from University of São Paulo, São Paulo, Brazil, in 2024. She is currently a Postdoctoral Researcher at University of São Paulo. Her research interests include power system analysis and control and renewable energy.

Renato M. Monaro received the B. Sc. degree in electrical engineering from University of São Paulo, São Paulo, Brazil, in 2007, and the Ph.D. degree from University of São Paulo, in 2013. He is currently an Associate Professor at University of São Paulo. His research interests include power system control and protection, voltage source converter based high-voltage direct current (HVDC-VSC) transmission, distributed generation, and renewable energy.

Gilney Damm received the B.Sc. degree in electronic engineering and the M.Sc. degree in automatic control from COPPE – Rio de Janeiro Federal University, Rio de Janeiro, Brazil, in 1995 and 1997, respectively, and the Ph. D. degree and Habilitation à Diriger des Recherches from the Paris-Saclay University, Gif-sur-Yvette, France, in 2001 and 2010, respectively. He was an Associate Professor with the Laboratoire des Signaux et Systémes (L2S), Paris-Saclay University. He is currently a Senior Research Scientist with the Laboratory Instrumentation, Modélisation, Simulation et Expérimentation (COSYS-IMSE), University Gustave Eiffel, Marne-la-Vallée, France. His research interests include nonlinear and adaptive control and observer applied to power systems (smart grid, super grid, and microgrid).

Cristiano M. Verrelli received the Ph. D. degree in system engineering from the University of Rome Tor Vergata, Rome, Italy, in 2005. He was a Visiting Scholar with the Laboratoire des Signaux et Systémes (L2S), Supelec, Gif-Sur-Yvette, France, and the Laboratoire Systémes Complexes (LSC), Evry, France, in 2004 and 2005, respectively, for the research project (Marie Curie training site): transient stabilization of power systems. He is currently an Associate Professor with the Department of Electronic Engineering, University of Rome Tor Vergata, Rome, Italy. He is also a Coordinator of the M.Sc. degree in mechatronics engineering. His research interests include dynamic system analysis, robust adaptive nonlinear control, and learning control theory with application to electrical machines, electrical vehicles, robots, physiological systems, epidemic models, and harmonic structures in human movement.